Unexplored signatures of magnetoelastic and isosymmetric metal-insulator phase transition in a rare-earth nickelate via mode crystallography

Harsh Kumar [1], Anar Singh [2], Jose Luis Martinez [3], Jose Antonio Alonso [3], and Saurabh Tripathi [1,*]

[1]*Department of Physics, Indian Institute of Technology (BHU), Varanasi, 221005, India*

[2]*Department of Physics, Faculty of Science, University of Lucknow, Lucknow 226007, India*

[3]*Instituto de Ciencia de Materiales de Madrid, C.S.I.C., Cantoblanco, E-28049 Madrid, Spain*

(Received 5 September 2022; revised 28 October 2022; accepted 14 November 2022; published 7 December 2022)

In the present work, we explored the interplay between the lattice and magnetic degrees of freedom in a rare-earth nickelate $EuNiO_3$, by carrying out temperature-dependent structural analysis in conjunction with distortion mode analysis. The temperature-dependent powder synchrotron x-ray diffraction (SXRD) studies revealed the presence of an orthorhombic *Pbnm* phase (tilt system $a_0^- a_0^- c_0^+$), with an elementary perovskite (pseudomonoclinic) cell, over the analyzed temperature range, i.e., 100–623 K. Further, we observed two distinct anomalies in the temperature-dependent evolution of pseudomonoclinic cell parameters (c_p/a_p, γ, V_{mono}) around 463 K and 200 K corresponding to respective isosymmetric metal-insulator transition temperature ($T_{M\text{-}I}$), and Neel temperature (T_N) linked with a volume gain at low temperatures dictating a magnetoelastic coupling in the system. We show the existence of two distinct pseudomonoclinic phases, viz., $\text{Mono}_{\text{metal}}$ ($T > T_{M\text{-}I}$) and $\text{Mono}_{\text{insulator}}$ ($T < T_{M\text{-}I}$), where the latter is more distorted than the former. The transition from $\text{Mono}_{\text{metal}}$ to $\text{Mono}_{\text{insulator}}$ at $T_{M\text{-}I}$ is reminiscent of a phase transition from orthorhombic (metallic) to monoclinic (insulating) phase, observed in other members of the rare-earth family. In addition, $T_{M\text{-}I}$ and T_N are clearly evident by the nonanalytical behavior of the condensed soft phonon modes amplitude corresponding to the zone boundary of the cubic Brillouin zone, viz., $X_5^+(q = 0, 1/2, 0)$ and $R_5^+(q = 1/2, 1/2, 1/2)$ as a function of temperature.

DOI: 10.1103/PhysRevB.106.214103

I. INTRODUCTION

We can induce a structural phase transition in a crystalline material by compositional engineering, temperature, pressure, electric field, crystallite size, and so on [1–3]. Generally, such phase transitions change the underlying symmetry of the material. The nature of such phase transitions could either be first or second order depending upon the group-subgroup relationship between the parent and daughter phases [4]. While the structural phase transitions involving change of space-group symmetry are very common in nature, there are several known examples of less commonly observed isostructural phase transition (ISPT) in which the lattice symmetry is preserved during the phase transition. These transitions are usually marked by the discontinuous changes in lattice constant, unit cell volume, dielectric constant, and so on [5,6]. In addition, such transitions may also exhibit a sharp change in the fractional coordinates of the atoms, which are directly related to displacement patterns of one or more modes corresponding to the irreducible representation (irreps) of the parent space group. Isostructural phase transitions were observed in various multiferroic systems such as $BiFeO_3$ [7,8], $BiFeO_3 - xPbTiO_3$ [5], $YMnO_3$ [9] etc. linked with transformation of one ferroelectric phase into another. Recently, an isostructural phase transition was observed in VO_2 which is accompanied by a metal-insulator transition [10].

An intriguing example to investigate the cooperative phenomenon between the electronic, magnetic, and lattice degrees of freedom could be found in the series of perovskite-structured rare-earth nickelates ($RNiO_3$), where R could be any rare-earth ranging from lutetium (Lu) to lanthanum (La) [11,12]. All members of the series (except $LaNiO_3$) exhibit a sharp metal-to-insulator transition as a function of temperature, which is accompanied by a symmetry-lowering transition from high-temperature metallic phase (orthorhombic *Pbnm*) to low-temperature insulating phase (monoclinic $P2_1/n$) with a significant conductivity change at M-I transition temperature ($T_{M\text{-}I}$) [13]. In the metallic region, conduction in nickelates happens due to overlapped p and d orbitals of oxygen and nickel, respectively, and the charge transfer mechanism given by $d_i^{3+}p_j^{2-} \leftrightarrow d_i^{2+}p_j^{1-}$ [12]. Just below $T_{M\text{-}I}$, nickelates behave as charge-transfer semiconductors. This insulating phase is known to have two nonequivalent Ni sites with slightly different average Ni-O bond lengths. This subtle Ni site splitting below $T_{M\text{-}I}$ results in a charge-ordered system and the charge disproportion among the two Ni sites is given by $2Ni^{3+} \rightarrow Ni^{3+\delta} + Ni^{3-\delta}$ [14,15]. In addition, all systems order antiferromagnetically at Neel temperature (T_N), which is the same as $T_{M\text{-}I}$ for Pr and Nd but lower than $T_{M\text{-}I}$ for smaller cations [15]. $EuNiO_3$, a member of the $RNiO_3$ series, exhibits three distinct phases, viz., paramagnetic metal, paramagnetic insulator, and antiferromagnetic insulator [12,16]. The transition from paramagnetic metal to paramagnetic insulator and then paramagnetic insulator to antiferromagnetic insulator occurs at $T_{M\text{-}I} \approx 460$ K and $T_N \approx$

*stripathi.phy@itbhu.ac.in

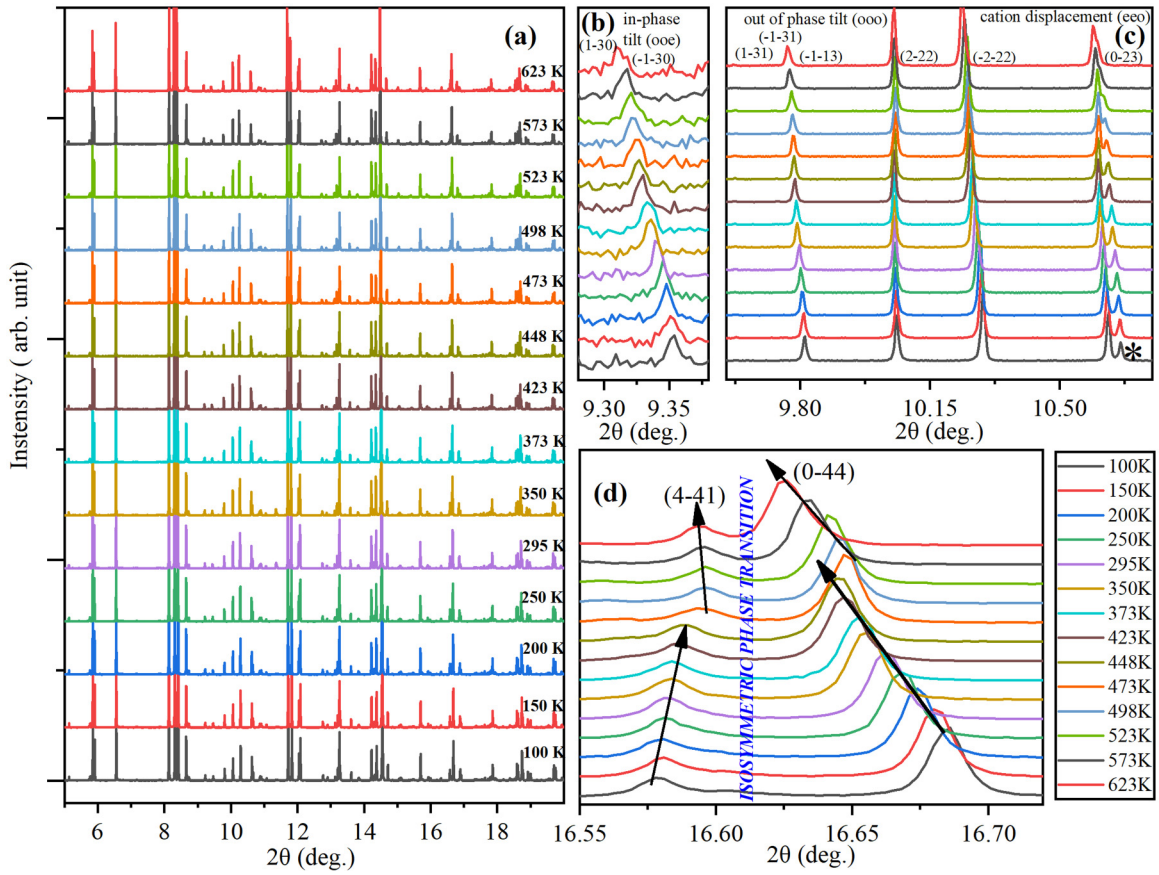

FIG. 1. The temperature-dependent evolution of x-ray diffraction profile of $EuNiO_3$ prepared at high pressure (3.5 GPa). Panels (b) and (c) represent the characteristic peaks of in-phase and out of phase rotation of adjacent NiO_6 octahedra and cation displacements, respectively. Panel (d) shows the temperature-dependent evolution of $(4\bar{4}1)$ and $(0\bar{4}4)$ peaks (indexing is done with respect to doubled pseudocubic cell). Sudden shift of both the peaks towards higher angle above 448 K indicates occurrence of a phase transition. The peak marked by * corresponds to minor impurity of NiO.

200 K, respectively [17]. The evidence of two nonequivalent Ni sites in the insulating phase were verified earlier with the aid of Mössbauer spectroscopy [18] and x-ray photoemission spectroscopy [19]. However, in our previous work, we observed a single orthorhombic *Pbnm* phase over the whole analyzed temperature range [20]. In this report, we expressed the orthorhombic supercell (SG: *Pbnm*; tilt system: $a_0^- a_0^- c_0^+$; cell size: $\sqrt{2}a_p \times \sqrt{2}b_p \times 2c_p$) into an elementary perovskite cell (pseudomonoclinic cell where $a_p = b_p > c_p$, pseudomonoclinic angle $\gamma \neq 90^\circ$). In our analysis, we identified two distinct pseudomonoclinic phases, viz., $\text{Mono}_{\text{metal}}$ ($T > T_{M\text{-}I}$) and $\text{Mono}_{\text{insulator}}$ ($T < T_{M\text{-}I}$), where the latter is more distorted structure as compared to the former as γ ($\text{Mono}_{\text{metal}}$) $> \gamma$ ($\text{Mono}_{\text{insulator}}$) and c_p/a_p ($\text{Mono}_{\text{metal}}$) $> c_p/a_p$ ($\text{Mono}_{\text{insulator}}$). The transition from $\text{Mono}_{\text{metal}}$ to $\text{Mono}_{\text{insulator}}$ may be considered similar to the symmetry-lowering metal-insulator phase transition from orthorhombic (metallic) to monoclinic (insulating) phase at $T_{M\text{-}I}$, observed in other members of the rare-earth series [21,22]. Apart from this, the signature of the magnetoelastic coupling associated with antiferromagnetic (AFM) transition is revealed by volume gain at low temperatures, which is also supported by discontinuities in pseudomonoclinic cell parameters (e.g., γ, c_p/a_p, etc.). Finally, we calculated the amplitude of various frozen phonon modes using temperature-dependent symmetry mode analysis. The anomalies observed in the amplitude of phonon modes, viz., $X_5^+(q = 0, 1/2, 0)$ and $R_5^+(q = 1/2, 1/2, 1/2)$, are used to substantiate the phase transitions.

II. EXPERIMENTAL SECTION

Europium nickelate ($EuNiO_3$) samples were synthesized under very high hydrostatic pressure (3.5 GPa) conditions in the presence of $KClO_4$. The synchrotron x-ray diffraction (SXRD) experiments were carried out on $EuNiO_3$ in the transmission mode on the BL04-MSPD beamline of the ALBA synchrotron (Barcelona, Spain) using the highest angular resolution as provided by the MAD setup. The beam energy was selected as 32 keV (0.38776 Å) to minimize the absorption. The complete experimental procedure has been given elsewhere [20]. Sequential x-ray diffraction patterns were collected over a wide range of temperatures from 100–623 K. The analysis of SXRD data was performed by Rietveld method using the FULLPROF suite [23]. For phonon mode decomposition we used AMPLIMODE software, available on the Bilbao crystallography server [24,25].

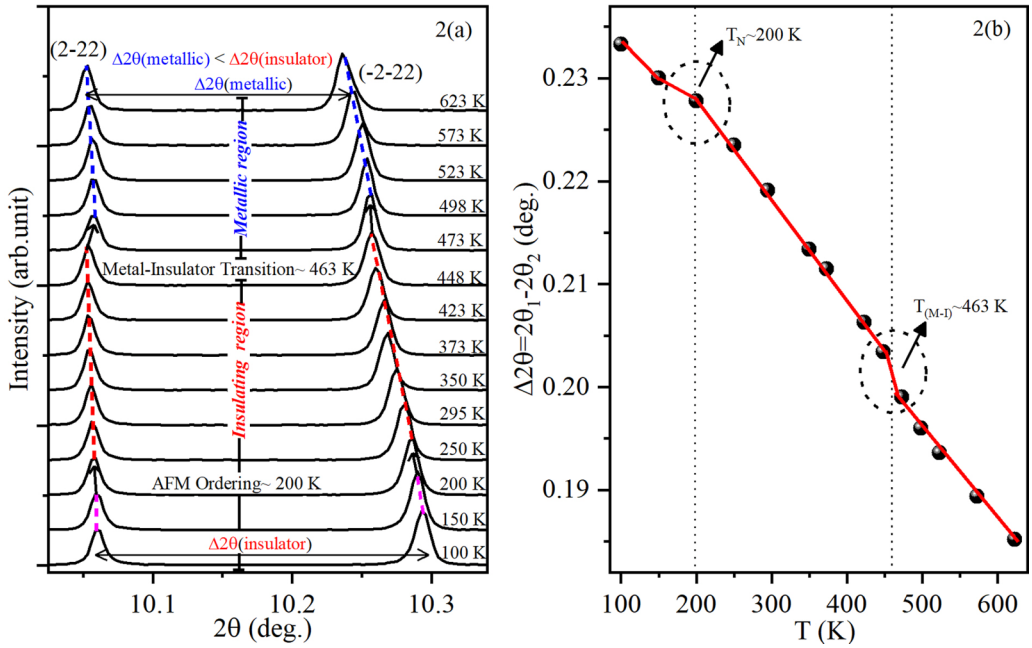

FIG. 2. (a) Zoomed view of $(2\bar{2}2)$ and $(\bar{2}\bar{2}2)$ reflections showing discontinuous shift around $T_{M\text{-}I}$ and T_N. (b) Evolution of separation between the $(2\bar{2}2)$ and $(\bar{2}\bar{2}2)$ reflections ($\Delta 2\theta$) with temperature. Two different slopes exist above and below the M-I phase transition and a change of slope around T_{M-I} indicates a remarkable increase in pseudomonoclinic distortion. Another change of slope around 200 K (Ni spin-ordering temperature) gives evidence of spin-lattice coupling in the system.

III. RESULTS AND DISCUSSION

A. Anomalies in crystal structure

The powder synchrotron x-ray diffraction (SXRD) data of $EuNiO_3$ was taken from Ref. [20]. Figure 1(a) shows the temperature-dependent evolution of the diffraction profile of $EuNiO_3$ in the selected 2θ range of 5°–20°. It was observed that the diffraction patterns do not change drastically as a function of temperature. There are two types of reflections present in the diffraction patterns of $EuNiO_3$, viz., main perovskite reflections and superlattice reflections. The main perovskite reflections arise due to the elementary perovskite cell while the superlattice reflections are due to the multipling of the elementary perovskite cell along one or more crystallographic axis [Figs. 1(b) and 1(c)]. We indexed all the reflections with respect to a doubled perovskite cell having cell size $2a_p$, $2b_p$, and, $2c_p$, where a_p, b_p, and c_p are the cell parameters of the elementary perovskite cell. There are a total of four distinct sets of hkl indices in the diffraction pattern, viz., even-even-even (eee), even-even-odd (eeo), odd-odd-even (ooe), and odd-odd-odd (ooo); the first set of indices corresponds to the main perovskite reflections, while the remaining three are associated with superlattice reflections. The reflections having indices of even-even-odd (eeo) type belong to antiparallel displacement of cations in adjacent layer perpendicular to [001] pseudocubic direction. On the other hand, reflections having indices odd-odd-odd (ooo) type and odd-odd-even (ooe) type arise due to out-of-phase and in-phase rotation of adjacent octahedra with respect to each other. The out-of-phase and in-phase octahedra rotations are driven by condensation of soft phonon modes corresponding to $R(q = 1/2, 1/2, 1/2)$ point and $M(q = 1/2, 1/2, 0)$ point of cubic Brillouin zone, respectively [26,27].

An elementary perovskite cell with orthorhombic structure gives a singlet peak for (hhh) type reflections. However, in case of $EuNiO_3$ with orthorhombic structure (SG: *Pbnm*, tilt system: $a_0^- a_0^- c_0^+$, cell size: $\sqrt{2}a_p \times \sqrt{2}b_p \times 2c_p$), we see two distinct peaks corresponding to (hhh)-type main perovskite reflections of elementary perovskite cell (i.e., pseudomonoclinic in our case with $a_p = b_p > c_p$, $\gamma \neq 90°$). For instance, the (222) reflection (indexing was done with respect to the doubled perovskite cell) in the diffraction pattern is split into two, viz., $(2\bar{2}2)$ and $(\bar{2}\bar{2}2)$, respectively. The separation between these two peaks ($\Delta 2\theta = 2\theta_1 - 2\theta_2$) is the measure of pseudomonoclinic distortion [see Fig. 2(a)]. Two discontinuities are clearly visible in the temperature-dependent evolution of $\Delta 2\theta$ at the metal-insulator transition temperature ($T_{M\text{-}I} \approx 463$ K) and AFM ordering temperature ($T_N \approx 200$ K), reported earlier [see Figs. 2(a) and 2(b)] [17,20]. An extreme scenario would be the overlapping of the two peaks ($\Delta 2\theta = 0$) resulting into a tetragonal unit cell with no pseudomonoclinic distortion.

The diffraction pattern shifts toward lower angles, indicating the increase in unit cell volume with an increase in temperature. However, $(0\bar{4}4)$ and $(4\bar{4}1)$ reflections show discontinuity in the peak positions between 473 K and 448 K [Fig. 1(d)]. Such a discontinuous shift of diffraction peaks indicates the onset of a phase transition between these two temperatures. On further decreasing the temperature, the intensity and the position of the peaks again change in a continuous manner. To ascertain the crystallographic structure of the phase, we carried out the Rietveld refinements of the SXRD data at various temperatures using the FULLPROF software package [23]. For 473 K and above, we considered the orthorhombic (SG: *Pbnm*) model, which has been reported for other members of $RNiO_3$ above the M-I transi-

tion. The orthorhombic *Pbnm* space group is an octahedrally tilted system with cell size $\sqrt{2}a_p \times \sqrt{2}b_p \times 2c_p$ and can be described by a simple tilt system $a_0^- a_0^- c_0^+$ in Glazer's notation [26,27]. In the *Pbnm* model, Eu and Ni occupy the Wyckoff sites $4c(x, y, 1/4)$ and $4b(1/2, 0, 0)$, while oxygen occupies two different Wyckoff sites $4c(x, y, 1/4)$ and $8d(x, y, z)$, respectively. This model fits very well for all the diffraction patterns above 473 K, as expected from previous results. For nickelates, it was observed that below the M-I transition, the crystallographic symmetry lowers to a monoclinic space group $(P2_1/n)$ [21,22]. The M-I transition temperature for $EuNiO_3$ is reported at 463 K [17]. Keeping this in mind, we checked the possibility of the monoclinic space group $(P2_1/n)$ at $\leqslant 448$ K. However, while refining with this space group, we have not seen any improvement in the fitting. Additionally, the absence of characteristic peak splitting of the $(0\bar{4}4)$ peak rules out the presence of the long-range-ordered monoclinic $(P2_1/n)$ phase. The sudden change in intensity and positions of the peaks such $(0\bar{4}4)$ and $(4\bar{4}1)$ indicates the occurrence of an isosymmetric phase transition (ISPT). Next, we tried to refine the structure with the same *Pbnm* model, which gave us satisfactory fit up to the lowest temperature. Hence, we conclude that the long-range symmetry is the same across the M-I and AFM transition temperature. Cinthia *et al.* [28] performed XAS studies on rare-earth nickelates with lighter lanthanides ($RNiO_3$; R = Pr, Nd, Eu, Y) where they argued that there are two different Ni sites present locally (at short-range) in insulating and metallic phase. In contrast, heavier lanthanides have a long-range monoclinic phase stable below the M-I phase transition [29]. From this, we infer that $RNiO_3$ with lighter lanthanides have a stable orthorhombic phase with *Pbnm* space group above and below the T_{M-I}. Therefore, our findings are consistent with the previous report and we believe $EuNiO_3$ may have a monoclinic local structure, but its average structure is orthorhombic below $T_{M\text{-}I}$. Hence, we conclude that the M-I transition in this system is isosymmetric. In general, ISPTs are accompanied by discontinuous changes in various physical properties such as specific heat, unit cell volume, resistivity, fractional atomic coordinates, and so on [5,30]. Different order parameters such as bond lengths, bond angle, atomic positions, unit cell volume, lattice parameters etc. were suggested [7,31,32].

At this point, it is worth mentioning that the orthorhombic supercell could be visualized from elementary perovskite (pseudomonoclinic) cell with lattice parameters a_p, b_p, c_p, and the unique angle between a_p and b_p (γ) whose relation with orthorhombic supercell parameters can be given as [33–35]

$$a_p = b_p = \tfrac{1}{2}[\sqrt{A^2 + B^2}], \tag{1}$$

$$c_p = \frac{C}{2}, \tag{2}$$

$$A^2 = a_p^2 + b_p^2 - 2a_p b_p \cos(\gamma), \tag{3}$$

$$B^2 = a_p^2 + b_p^2 + 2a_p b_p \cos(\gamma)'. \tag{4}$$

Here $a_p = b_p$, hence Eq. (3) will give

$$\sin(\gamma/2) = \frac{A}{2a_p}. \tag{5}$$

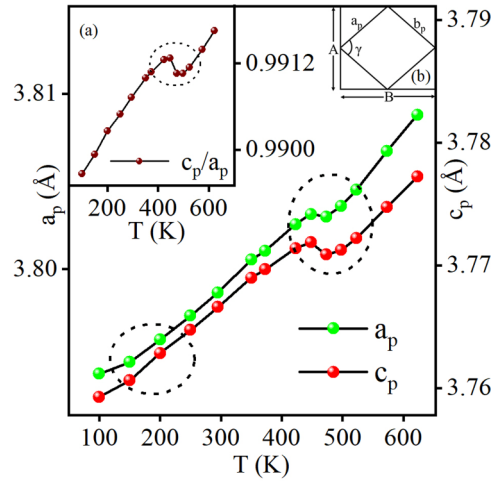

FIG. 3. Temperature-dependent evolution of pseudomonoclinic cell parameters. The inset (a) shows the sudden change of c_p/a_p between 448 K and 473 K. The inset (b) shows the transformation of the orthorhombic supercell into a pseudomonoclinic cell.

Here, a_p, b_p, and c_p are cell parameters of the pseudomonoclinic cell while A, B, and C are cell parameters of the orthorhombic supercell. The pseudomonoclinic angles are $(\gamma) = 90^\circ - \delta$ and $(\gamma)' = 90^\circ + \delta$, where δ is a small deviation from 90°. The temperature-dependent variation of the elementary perovskite (pseudomonoclinic) cell parameters $a_p = b_p$, c_p and the pseudomonoclinic angle γ of $EuNiO_3$ can be obtained by Rietveld-refined orthorhombic unit cell parameters (A, B, C).

It is interesting to observe that, although the elementary perovskite cell exhibits pseudomonoclinicity over the temperature range (100–623 K), it enhanced as the temperature decreases, with an anomaly at the M-I transition (Fig. 3). The abrupt change in pseudomonoclinic cell parameters at T_{M-I} is indicative of the first-order isosymmetric metal-insulator phase transition. Figure 4 depicts the variation of

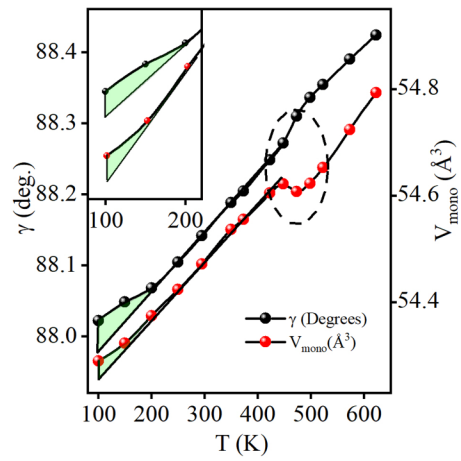

FIG. 4. Temperature-dependent evolution of pseudomonoclinic angle γ and volume V_{mono}. A drastic change in slope of γ vs T around M-I transition, point out the change in distortion of the pseudomonoclinic cell. The inset shows an expanded view of low-temperature region of both curves.

pseudomonoclinic angle (γ) and volume (V_{mono}) with temperature. A sharp anomaly at $T_{\text{M-I}}$ is clearly visible in the pseudomonoclinic cell parameters (see Figs. 3 and 4), separating two pseudomonoclinic regions, viz., (a) metallic pseudomonoclinic region above $T_{\text{M-I}}$ and (b) insulating pseudomonoclinic region below $T_{\text{M-I}}$. The two regions correspond to two distinct pseudomonoclinic phases, viz., $\text{Mono}_{\text{metal}}$ and $\text{Mono}_{\text{insulator}}$, respectively, where the latter is more distorted than the former since γ ($\text{Mono}_{\text{metal}}$) $>$ γ ($\text{Mono}_{\text{insulator}}$) and c_p/a_p ($\text{Mono}_{\text{metal}}$) $>$ c_p/a_p ($\text{Mono}_{\text{insulator}}$). We find that these two phases, viz., $\text{Mono}_{\text{metal}}$ and $\text{Mono}_{\text{insulator}}$ are in close analogy with the orthorhombic (metallic) and monoclinic (insulating) structures discovered in other members of the rare-earth nickelates [21,22]. The transition from $\text{Mono}_{\text{metal}}$ to $\text{Mono}_{\text{insulator}}$ resembles the symmetry-lowering metal-insulator transition from high-temperature orthorhombic (metallic) phase to low-temperature monoclinic (insulator) phase at $T_{\text{M-I}}$, generally observed in rare-earth nickelates, thus establishing a correspondence between the two transitions. Moreover, an anomaly at $T \approx 200$ K is observed in the pseudomonoclinic angle γ, which coincides with the Neel temperature (T_N) reported earlier [17]. Furthermore, below 200 K, there is a change in V_{mono} versus T slope without a discernible change in the magnitude of V_{mono}. This demonstrates the interconnection between magnetic and lattice degrees of freedom suggesting a spin-phonon (magnetoelastic) coupling in the system. Such magnetoelastic coupling is typically seen when the thermal expansion of lattice deviates from Gruiensen's law. This law accounts for phonons as a contributor to the thermal expansion of lattice parameters [36]. From Fig. 4 it is very clear that below T_N, $EuNiO_3$ experiences an additional contribution to the thermal expansion of magnetoelastic origin. Such a contribution could be attributed to a long-range antiferromagnetic ordering due to the existence of magnetic moment instabilities and related structural transition associated with the magnetic transition. However, data points were insufficient to separate the thermal and magnetic contributions to volume expansion.

Both the space-group symmetry and the occupied Wyckoff positions are preserved in the isostructural phase transition (ISPT) in $EuNiO_3$. To gain insight into ISPT, we examined the temperature-dependent evolution of atomic coordinates. In our *Pbnm* model, Ni has fixed position while Eu and O atoms have variable fractional coordinates. Owning to the higher atomic number of the Eu atom, the information content regrading the Eu atom in x-ray diffraction data is significantly more than the O atom. Accordingly, we considered the temperature-dependent evolution of Eu coordinates in our analysis to explore the ISPT and AFM transitions. Figure 5 depicts the variation of the x and y coordinates of the Eu atom with temperature. Across the M-I transition and AFM ordering, both coordinates change in a nonanalytical way. The irregularities in the the displacement of the cations are very well reflected in the diffraction pattern in even-even-odd (eeo) type reflections for, e.g., $(4\bar{4}1)$ (see Fig. 1). We will now use distortion-mode analysis to ascertain the possible role of condensation of soft phonon modes in stabilizing the low symmetry phase.

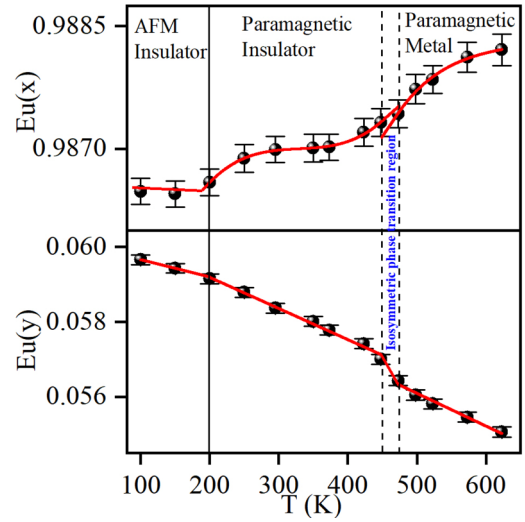

FIG. 5. Temperature-dependent evolution of fractional x and y coordinates of Eu atom obtained from Rietveld refinement using powder synchrotron x-ray diffraction data. Discontinuities around T_N and $T_{M\text{-}I}$ are clearly visible in both the plots.

B. Distortion mode analysis

The orthorhombic *Pbnm* phase of $EuNiO_3$ could be described as the superposition of various distortion modes of an ideal cubic structure [35]. Distortion modes that lead to the low symmetry phase are considered as primary modes, while other symmetrically permitted modes are considered as secondary modes. The amplitude of primary distortion modes act as an order parameter to describe the phase transition(s) and anomalies in its temperature-dependent evolution gives the signature(s) of the structural phase transition(s) [37–39]. The low symmetry distorted structure could be derived from a high symmetry structure via condensation of one or more soft phonon modes. Moreover, a group-subgroup relation must exist between the parent and low symmetry structure and the low symmetry structure can be visualized as a high symmetry structure plus a static symmetry breaking structural distortion [24,25]. Mathematically this could be written as

$$r(\mu, i) = r_o(\mu, i) + u(\mu, i), \tag{6}$$

where $r_o(\mu, i)$ are the positions of μ (μ= 1,2,3,...,) atoms within the asymmetric unit of the parent structure corresponding to space group G expressed in the low-symmetry setting, $r(\mu, i)$ are the positions of μ atoms in the low-symmetry structure corresponding to space group H, which is a subgroup of group G, $u(\mu, i)$ are the static atomic distortions present in the low-symmetry structure, respectively. These distortions can be seen as a contribution from different frozen phonon modes whose symmetries are given by the irreducible representations of the parent space group. For quantifying the distortion modes, we used AMPLIMODES, a program available on the Bilbao crystallography server [24,25]. Given the high- and low-symmetry structures, AMPLIMODE calculates the amplitude and polarization vectors of the distortion modes corresponding to different

TABLE I. Wyckoff sites occupied by atoms in low- and high-symmetry structures along with phonon modes responsible for symmetry breaking.

Wyckoff site splitting		
SG:$Pm\bar{3}m$	**Symmetry breaking modes**	**SG**:*Pbnm*
Eu **1a**	X_5^+(Eu), R_5^+(Eu)	Eu **4c**
Ni **1b**	-	Ni **4b**
O **3d**	R_4^+, M_3^+, X_5^+(O), R_5^+(O), M_2^+	O1 **4c**, O2 **8d**

symmetry modes in the structure. The amplitudes of the distortion modes are used as order parameters to describe the symmetry breaking transition (for, e.g., $Pm\bar{3}m \rightarrow Pbnm$ in our case). For calculating the amplitudes of various distortion modes, responsible for driving the phase transitions, we need (i) polarization vectors corresponding to respective distortion mode, (ii) lattice parameters of the reference structure, (iii) Wyckoff site multiplicity, and (iv) displacement of atoms in the low-symmetry phase with respect to their positions in undistorted reference structure. Here, the polarization vectors are useful in defining the corelated atomic displacements that are involved in each mode and provide valuable information for understanding the structural phase transitions of displacive type.

As input for the AMPLIMODES, we used the primitive cubic cell (SG: $Pm\bar{3}m$) and orthorhombic cell (SG:*Pbnm*) as high and low symmetry structures, respectively [40]. Eu, Ni, and O atoms occupy 1(b) (0.5,0.5,0.5), 1(a) (0,0,0), and 3(d) (0.5,0,0) Wyckoff sites, respectively, in the high symmetry cubic phase with perovskite structure ABO_3. The transition from cubic phase to orthorhombic phase occurs via splitting of the Wyckoff site in the fashion given in Table I.

The static displacement resulting from synergistic coupling of two primary modes, viz., R_4^+ and M_3^+ leads to a symmetry breaking transition: $Pm\bar{3}m \rightarrow Pbnm$. These two order parameters are linked with R $(q = 1/2, 1/2, 1/2)$ and M $(q = 1/2, 1/2, 0)$ point of the cubic Brilluion zone and result in out-of-phase and in-phase rotations of adjacent octahedra, respectively [3,39,41,42]. Two other secondary modes with considerably high amplitudes, viz., $X_5^+(q = 0, 1/2, 0)$ and $R_5^+(q = 1/2, 1/2, 1/2)$ primarily contribute to displacements of the A site cation. Figure 6 depicts the schematic representation of the seven distortion modes involved in the orthorhombic *Pbnm* phase. For clear representation, two different schematics were used to show the displacement pattern of modes involving more than one atom for, e.g., Figs. 6(a) and 6(b) for R_5^+ and Figs. 6(c) and 6(d) for X_5^+. In Fig. 7, we plotted the temperature-dependent evolution of the R_5^+(Eu) and X_5^+(Eu) modes' amplitude. The phonon-mode amplitudes of these modes increase with the decrease in temperature, suggestive of enhancement in distortion at low temperatures. Further, the anomalies in mode amplitudes around $T_{\text{M-I}} \approx$ 463 K and $T_{\text{N}} \approx 200$ K, corroborate the two transitions. These two modes are of particular importance in our case since we are using synchrotron x-rays to probe the crystal structure, which is more susceptible to heavier atoms due to their high electron density. Hence x-rays can be used to capture the subtle displacement of Eu atoms. Furthermore, neutron diffraction experiment is not feasible in the case of $EuNiO_3$

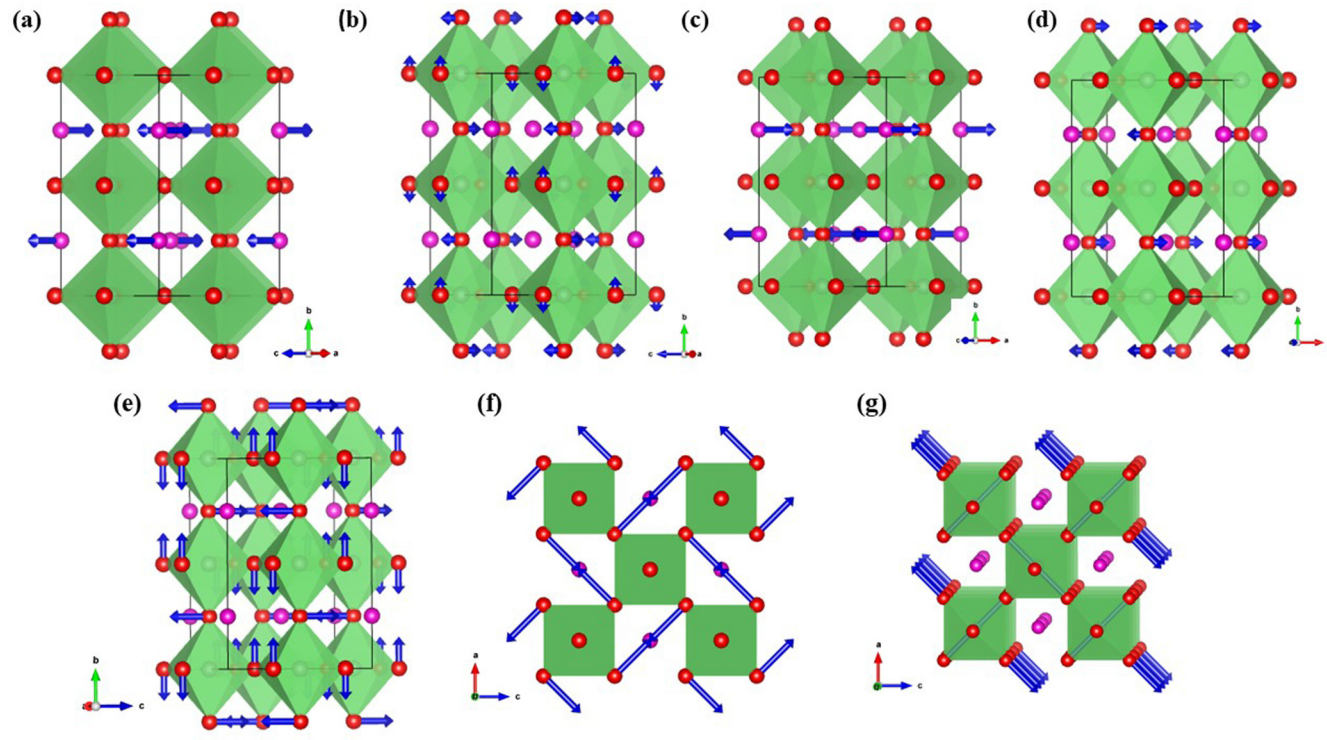

FIG. 6. Schematic representation of the atomic displacement pattern of various distortion modes involved in symmetry breaking transition $Pm\bar{3}m \rightarrow Pbnm$: (a) R_5^+(Eu), (b) R_5^+(O), (c) X_5^+(Eu), (d) X_5^+(O), (e) R_4^+, (f) M_3^+, and (g) M_2^+. Irreps having contribution from more than one atom (X_5^+ and R_5^+) are represented separately.

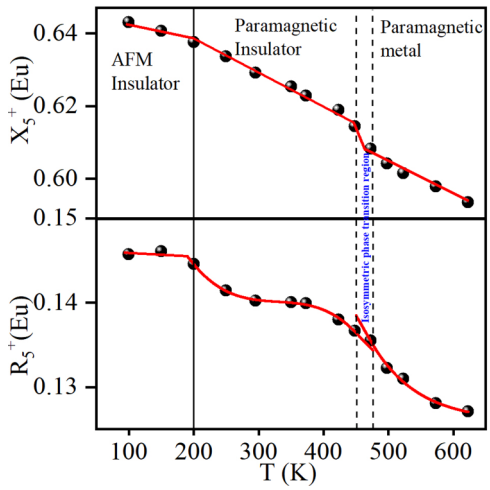

FIG. 7. Temperature-dependent evolution of X_5^+(Eu) and R_5^+(Eu) phonon modes amplitude. These two modes are responsible for displacement of Eu atom from its position in an ideal cubic structure.

due to the high absorbing nature of Eu atoms. In the light of our results, we show that the structural phase transitions can be probed efficiently with the modes associated with the *A* site cation.

IV. CONCLUSION

In this work, we presented strong evidences for an isosymmetric metal-insulator transition by expressing the conventional orthorhombic supercell into an elementary perovskite (pseudomonoclinic) cell for a rare-earth nickelate $EuNiO_3$. We identified two distinct pseudomonoclinic phases, viz., $Mono_{metal}$ ($T > T_{M\text{-}I}$) and $Mono_{insulator}$ ($T < T_{M\text{-}I}$) where the latter is comparatively more distorted. The $Mono_{metal}$ and $Mono_{insulator}$ are similar to the orthorhombic and monoclinic structures frequently observed in the other members of the rare-earth family. The anomalies observed in the temperature-dependent evolution of pseudomonoclinic cell parameters (a_p/c_p, γ, V_{mono}) are very well corroborated with the metal-insulator transition temperature ($T_{M\text{-}I}$) and Neel temperature (T_N). The volume gain by elementary perovskite (pseudomonoclinic) cell below Neel's temperature gives evidence of spin-phonon coupling. The fractional atomic coordinates of the Eu atom obtained by Rietveld analysis, and the amplitude of corresponding phonon modes (X_5^+ and R_5^+) change in a nonanalytical manner at $T_{M\text{-}I}$ and T_N. The anomalies in the amplitude of phonon modes at Neel temperature also suggest spin-lattice interactions in the system. The new insight into metal-insulator (M-I) and antiferromagnetic (AFM) transitions has been given using rigorous crystallography of supercell as well as elementary perovskite cell coupled with symmetry mode analysis. Our results show the advantage of using an elementary (pseudomonoclinic) cell description of an orthrhombic supercell for quantifying various structural distortions driven by symmetry-adapted phonon modes. The presence of magnetoelastic coupling in the system provides an extra degree of freedom for device fabrication.

ACKNOWLEDGMENTS

This research was partially funded by the Spanish Ministry of Science and Innovation, MCIN/AEI/10.13039/501100011033/, with the Projects No. PID2021-122477OB-I00 and No. TED2021-129254B-C22. S.T. acknowledges financial assistance from DST-SERB, Government of India (Grant No. CRG/2021/006000).

[1] X. Luo, L. Wu, J. Huang, and M. Zhou, J. Appl. Phys. **130**, 245102 (2021).
[2] A. K. Singh, D. N. Dubey, G. Singh, and S. Tripathi, Europhys. Lett. **130**, 36002 (2020).
[3] A. K. Singh, D. N. Dubey, G. Singh, and S. Tripathi, Appl. Phys. Lett. **116**, 232902 (2020).
[4] P. Toledano and J.-C. Toledano, *Landau Theory Of Phase Transitions, The: Application To Structural, Incommensurate, Magnetic, And Liquid Crystal Systems* Vol. 3, (World Scientific, Singapore, 1987).
[5] S. Bhattacharjee, K. Taji, C. Moriyoshi, Y. Kuroiwa, and D. Pandey, Phys. Rev. B **84**, 104116 (2011).
[6] A. Singh, A. Senyshyn, H. Fuess, T. Chatterji, and D. Pandey, Phys. Rev. B **83**, 054406 (2011).
[7] R. Zeches, M. Rossell, J. Zhang, A. Hatt, Q. He, C.-H. Yang, A. Kumar, C. Wang, A. Melville, C. Adamo *et al.*, Science **326**, 977 (2009).
[8] S. Lisenkov, D. Rahmedov, and L. Bellaiche, Phys. Rev. Lett. **103**, 047204 (2009).
[9] S. Tripathi and V. Petkov, Appl. Phys. Lett. **102**, 061909 (2013).
[10] D. Lee, B. Chung, Y. Shi, G.-Y. Kim, N. Campbell, F. Xue, K. Song, S.-Y. Choi, J. Podkaminer, T. Kim *et al.*, Science **362**, 1037 (2018).
[11] M. L. Medarde, J. Phys.: Condens. Matter **9**, 1679 (1997).
[12] G. Catalan, Phase Transitions **81**, 729 (2008).
[13] J. Goodenough and P. Raccah, J. Appl. Phys. **36**, 1031 (1965).
[14] M. T. Fernández-Díaz, J. Alonso, M. Martínez-Lope, M. Casais, J. García-Muñoz, and M. Aranda, Phys. B: Condens. Matter **276**, 218 (2000).
[15] Y. M. Klein, M. Kozłowski, A. Linden, P. Lacorre, M. Medarde, and D. J. Gawryluk, Cryst. Growth Des. **21**, 4230 (2021).
[16] J. Alonso, M. Martınez-Lope, and I. Rasines, J. Solid State Chem. **120**, 170 (1995).
[17] J. B. Torrance, P. Lacorre, A. I. Nazzal, E. J. Ansaldo, and C. Niedermayer, Phys. Rev. B **45**, 8209(R) (1992).
[18] A. Caytuero, H. Micklitz, M. M. Abd-Elmeguid, F. J. Litterst, J. A. Alonso, and E. M. Baggio-Saitovitch, Phys. Rev. B **76**, 193105 (2007).
[19] K. Bilewska, E. Wolna, M. Edely, P. Ruello, and J. Szade, Phys. Rev. B **82**, 165105 (2010).

[20] F. Serrano-Sanchez, J. L. Martínez, F. Fauth, and J. A. Alonso, Dalton Transactions **50**, 7085 (2021).
[21] A. Muñoz, J. Alonso, M. Martínez-Lope, and M. Fernández-Díaz, J. Solid State Chem. **182**, 1982 (2009).
[22] F. Serrano-Sánchez, F. Fauth, J. L. Martínez, and J. A. Alonso, Inorg. Chem. **58**, 11828 (2019).
[23] J. Rodríguez-Carvajal, Phys. B: Condens. Matter **192**, 55 (1993).
[24] D. Orobengoa, C. Capillas, M. I. Aroyo, and J. M. Perez-Mato, J. Appl. Crystallogr. **42**, 820 (2009).
[25] J. Perez-Mato, D. Orobengoa, and M. Aroyo, Acta Crystallogr. A: Found. Crystallogr. **66**, 558 (2010).
[26] A. M. Glazer, Acta Crystallogr. B: Struct. Crystallogr. Cryst. Chem. **28**, 3384 (1972).
[27] A. Glazer, Acta Crystallogr., Sect. A: Cryst. Phys., Diffr., Theor. Gen. Crystallogr. **31**, 756 (1975).
[28] C. Piamonteze, H. C. N. Tolentino, A. Y. Ramos, N. E. Massa, J. A. Alonso, M. J. Martínez-Lope, and M. T. Casais, Phys. Rev. B **71**, 012104 (2005).
[29] J. A. Alonso, M. J. Martínez-Lope, M. T. Casais, J. L. García-Muñoz, and M. T. Fernández-Díaz, Phys. Rev. B **61**, 1756 (2000).
[30] J. F. Scott, Adv. Mater. **22**, 2106 (2010).
[31] A. Singh, V. Pandey, R. K. Kotnala, and D. Pandey, Phys. Rev. Lett. **101**, 247602 (2008).
[32] V. Ranjan, S. Bin-Omran, L. Bellaiche, and A. Alsaad, Phys. Rev. B **71**, 195302 (2005).
[33] S. Tripathi, A. Kumar, S. Shirodkar, M. Yashima, U. Waghmare, and D. Pandey, arXiv:1408.0335.
[34] J. Tellier, B. Malic, B. Dkhil, D. Jenko, J. Cilensek, and M. Kosec, Solid State Sci. **11**, 320 (2009).
[35] A. Tripathi, D. N. Dubey, H. Kumar, and S. Tripathi, J. Appl. Crystallogr. **55**, 1446 (2022).
[36] M. Ibarra Garcia and S. Elsheikhi, in *Reference Module in Materials Science and Materials Engineering* (Elsevier, Amsterdam, 2016).
[37] C. J. Howard and H. T. Stokes, Acta Crystallogr. Sect. B: Struct. Sci. **60**, 674 (2004).
[38] C. J. Howard and H. T. Stokes, Acta Crystallogr. A: Found. Crystallogr. **61**, 93 (2005).
[39] C. J. Howard and M. A. Carpenter, Acta Crystallogr., Sect. B: Struct. Sci. **66**, 40 (2010).
[40] D. J. Gawryluk, Y. M. Klein, T. Shang, D. Sheptyakov, L. Keller, N. Casati, P. Lacorre, M. T. Fernández-Díaz, J. Rodríguez-Carvajal, and M. Medarde, Phys. Rev. B **100**, 205137 (2019).
[41] H. T. Stokes, E. H. Kisi, D. M. Hatch, and C. J. Howard, Acta Crystallogr. Sect. B: Struct. Sci. **58**, 934 (2002).
[42] D. N. Dubey, G. Singh, A. K. Singh, and S. Tripathi, Europhys. Lett. **140**, 26003 (2022).